AGU PUBLICATIONS

JGR

Journal of Geophysical Research: Solid Earth

RESEARCH ARTICLE
10.1002/2015JB012158

Key Points:
- Fault composite slip monitoring
- Hydraulic transmissivity increase with shear
- Diffusivity changes related to complex effects off the slip plane

Correspondence to:
Y. Guglielmi,
guglielmi@cerege.fr

Citation:
Guglielmi, Y., D. Elsworth, F. Cappa, P. Henry, C. Gout, P. Dick, and J. Durand (2015), In situ observations on the coupling between hydraulic diffusivity and displacements during fault reactivation in shales, *J. Geophys. Res. Solid Earth*, *120*, doi:10.1002/2015JB012158.

Received 28 APR 2015
Accepted 20 OCT 2015
Accepted article online 22 OCT 2015

©2015. American Geophysical Union. All Rights Reserved.

In situ observations on the coupling between hydraulic diffusivity and displacements during fault reactivation in shales

Yves Guglielmi[1], Derek Elsworth[2], Frédéric Cappa[3,4], Pierre Henry[1], Claude Gout[5], Pierre Dick[6], and Jérémie Durand[7]

[1]CEREGE, Aix-Marseille University–CNRS–IRD, Marseille, France, [2]Department of Energy and Mineral Engineering, Pennsylvania State University, University Park, Pennsylvania, USA, [3]Géoazur, University of Nice Sophia Antipolis–CNRS–IRD–OCA, Sophia-Antipolis, France, [4]Institut Universitaire de France, Paris, France, [5]Exploration and Production, Research and Development, TOTAL, Pau cedex, France, [6]PRP-DGE/SRTG/IRSN, Laboratoire d'Etude et de Recherche sur les Transferts et les Interactions dans les Sols, Fontenay-aux-Roses CEDEX, France, [7]SITES S.A.S., Espace Européen, Ecully, France

Abstract Key questions in fault reactivation in shales relate to the potential for enhanced fluid transport through previously low-permeability aseismic formations. Here we explore the behavior of a 20 m long N0-to-170°, 75-to-80°W fault in shales that is critically stressed under a strike-slip regime ($\sigma_1 = 4 \pm 2$ MPa, horizontal and N162° ± 15°E, $\sigma_2 = 3.8 \pm 0.4$ MPa and $\sigma_3 = 2.1 \pm 1$ MPa, respectively 7–8° inclined from vertical and horizontal and N72°). The fault was reactivated by fluid pressurization in a borehole using a straddle packer system isolating a 2.4 m long injection chamber oriented-subnormal to the fault surface at a depth of 250 m. A three-dimensional displacement sensor attached across the fault allowed monitoring fault movements, injection pressure and flow rate. Pressurization induced a hydraulic diffusivity increase from ~2×10^{-9} to ~10^3 $m^2 s^{-1}$ associated with a complex three-dimensional fault movement. The shear (*x*-, z-) and fault-normal (*y*-) components (U_x, U_y, and U_z) = (44.0×10^{-6} m, 10.5×10^{-6} m, and 20.0×10^{-6} m) are characterized by much larger shear displacements than the normal opening. Numerical analyses of the experiment show that the fault permeability evolution is controlled by the fault reactivation in shear related to Coulomb failure. The large additional fault hydraulic aperture for fluid flow is not reflected in the total normal displacement that showed a small partly contractile component. This suggests that complex dilatant effects estimated to occur in a plurimeter radius around the injection source affect the flow and slipping patch geometries during fault rupture, controlling the initial slow slip and the strong back slip of the fault following depressurization.

1. Introduction

Fluid pressurization may trigger the reactivation of faults, affecting the transport characteristics of the formation. These are crucial processes in understanding how fluids may be contained by seal layers, containing the migration of hydrocarbons at the basin scale or contributing to loss of integrity of reservoir/seal systems [*Rutqvist et al.*, 2007]. This is also a key question in understanding the role of fluids in faulting at the crustal scale, for example, at subduction zones through the development of excess pore pressures in low-permeability sediments trapped in active accretionary wedges [*Boutt et al.*, 2012]. Evidence for rapid flow from seismogenic depths channeled along thrusts have been obtained in IODP drill holes on the Cascadia margin [*Davis et al.*, 1995], and a number of physical models constrain the relationships between transient pore pressures and seismic or aseismic slip [*Muir-Wood and King*, 1993; *Ge and Stover*, 2000; *Henry*, 2000; *Davis et al.*, 2001; *Wang et al.*, 2001; *Husen and Kissling*, 2001]. The relationships between fluid flow and fault slip pose a ubiquitous question in understanding how fault permeability evolves during fault movement.

In the laboratory, the evolution of permeability in faults as a function of shear appears to be a complex issue since it remains dependent on the applied effective normal stresses, and which in turn moderate dilatancy related to fault surface asperities [*Olsson and Brown*, 1993; *Archambault et al.*, 1997] and the formation of gouge [*Faoro et al.*, 2009]. Real faults at field scale cannot be considered as a single continuous surface but occupy a rock volume typically with complex deformation structures schematically composed of one or multiple fault cores and damaged/fractured zones [*Gudmundsson et al.*, 2001, 2010; *Mitchell and Faulkner*, 2009; *Faulkner et al.*, 2010]. Most of the sliding deformation is accommodated in the fault core that consists primarily of breccia,

gouge, and multiple sliding surfaces [*Zhang et al*., 1999; *Bruhn et al*., 1994]. The damaged zone can be considered a complex fractured zone, where some fractures may have experienced shearing, dilation, and wear. Such structural heterogeneity of fault zones induces a strongly heterogeneous permeability field through the fault zone, the core usually being considered much less permeable than the fault damage zone [*Caine et al*., 1996; *Evans et al*., 1997]. Laboratory testing and numerical modeling of the effects of poroelastic stressing of such composite materials show that permeability can increase over 2-to-3 orders of magnitudes prior to macroscopic failure [*Wibberley and Shimamoto*, 2003; *Mitchell and Faulner*, 2008; *Cappa*, 2009]. Nevertheless, using laboratory cores to infer field-scale permeability structures remains a key question since the case of significant deviatoric stress fluid flow in laboratory core scale microcracks is poorly representative of large scale flow in fractures [*Coyle and Zoback*, 1988; *Brown and Bruhn*, 1998].

Fault zones in the shale formations of Tournemire (France) are characterized by a reorganization of phyllosilicate-rich materials [*Charpentier et al*., 2003; *Constantin et al*., 2007] combined with an important capacity of self-healing by swelling of clay minerals and in sealing through the redistribution of calcite in freshly opened discontinuities [*Constantin et al*., 2004]. As a result of these dual mechanisms, faults in these shales are presumed of low permeability—equal to or only marginally higher than that of the intact rock. Nevertheless, the concentration of calcite veins in the fault zones suggests that fluid migration is concurrent with faulting. Similar permeabilities of 10^{-18}–10^{-16} m^2 have been measured in the damage zone of the Chelungpu active fault affecting silty shales [*Doan et al*., 2006]. These values are at most 100 times larger than the values obtained on intact core samples from the host rock [*Chen et al*., 2005], highlighting the strong potential effect of faults reactivation in the enhancement of permeability in shales. The key questions are as follows: which mechanisms of fault opening and slip favor permeability increase, therefore enhancing fluid leakage in very low permeability shales? How large can the permeability increase become?, and what feedback exist in triggering fault slip instability?

The following shows results of a fault reactivation experiment, using an instrumental device that allows the synchronous monitoring of fault movement during pressurization by water in the borehole interval the fault zone. This represents an attempt to measure in situ evolution of permeability contemporaneous with induced slip. We first describe the experimental protocol and then report and analyze the results of a fault reactivation experiment conducted on an ~20 m long satellite fault-spur to the fractured damage zone of a 500 m long fault in Toarcian shale adjacent to the Institute for Radiological Protection and Nuclear Safety (IRSN) Tournemire underground research laboratory (URL) [*Cabrera et al*., 2001]. We analyze the contributions of nonshear and shear displacements on permeability evolution in the fault, and using a simple three-dimensional numerical representation of hydro-mechanical coupling explores the relationship between fluid pressure, flow rate, and fault movement. We discuss (1) the sensitivity/accuracy of this field protocol, (2) the principal mechanisms controlling the observed response, and (3) the respective influence of stress and initial properties on fluid induced fault reactivation.

2. In Situ Experimental Setting

2.1. Fault Geology

The Tournemire URL is located in southern France (Figure 1). This site was originally selected by the French Institute for Radiological Protection and Nuclear Safety (IRSN) to study the migration-confinement potential of a 250 m thick Toarcian-Domerian shale formation [*Cabrera et al*., 1999]. The Tournemire shale features typical anisotropic textures induced by compaction. The mineral composition that is relatively homogeneous for the upper Toarcian section [*Tremosa et al*., 2012] contains 39–51% phyllosilicates (smectite, illite, kaolinite, chlorite, and mica), 24–36% quartz, 16–17% carbonate (bioclasts and diagenetic calcite are predominant and dolomite and siderite are in small proportions), and 4–8% of K-feldspars [*Charpentier et al*., 2003]. The shale is characterized by a low porosity (8–12%) with a water content of 3.5–5% at natural saturation and a coefficient of permeability of 10^{-11}-to-10^{-15} m/s [*Bonin*, 1998; *Boisson et al*., 2001; *Hedan et al*., 2011].

The fault in this study is a small ~20 m long satellite fault-spur to the main damage zone of a larger fault zone that is exposed in the underground laboratory (Figure 1a). The offset of the fault is ~10 m, and the fault intersects the 250 m thick Toarcian shale formation almost horizontally [*Constantin et al*., 2004]. The tested fault-spur is a N0-to-170°, 75-to-80°W left-lateral strike-slip fault. The stress state was determined with a series of leak off tests performed in an ~180 m deep vertical borehole at different depths (to estimate stress variations with depth) and located ~50 m from the current experiment [*Cornet*, 2000]. Leak off tests confirm the strike-slip

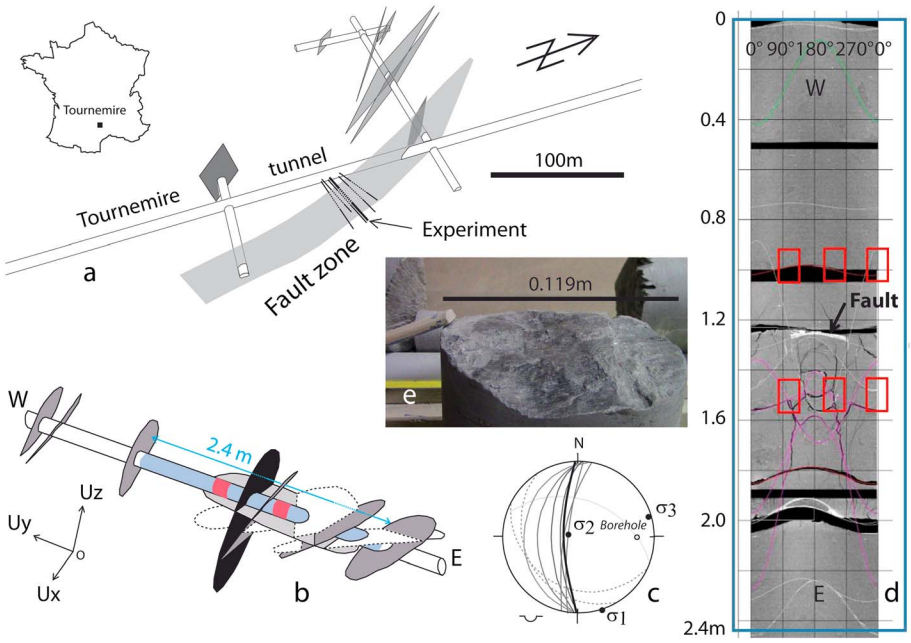

Figure 1. (a) Tournemire Underground Research Laboratory crosscutting the studied fault zone and experiment location. (b) Structures distribution along the injection borehole (injection intervals is shown in blue, red intervals correspond to the location of the SIMFIP probe displacement sensor anchors). (c) Stereographic projection of the main fracture/fault plane families that characterize the tested interval and principal stresses determined by *Cornet* [2000]. (d) CT-scan view of the surface (0–360° developed view where the 0–180° lines are contained in the vertical plane) of the core corresponding to the test interval. Red rectangles show the anchoring zones of the displacement instrument. Blue rectangle shows the limits of the injection chamber. Black stripes are voids corresponding to sampling zones. (e) View of the main fault plane surface (which is pointed with the arrow in Figure 1d).

regime with a stress regime of $\sigma_1 = 4 \pm 2$ MPa, horizontal and oriented N162° ± 15°E, $\sigma_2 = 3.8 \pm 0.4$ MPa, 7–8° inclined from vertical in the N72° direction and $\sigma_3 = 2.1 \pm 1$ MPa, 7–8° inclined from horizontal in the N72° direction (Figures 1b and 1c).

The injection experiments were conducted in a 30 m long and 0.146 m diameter borehole drilled from the Tournemire tunnel and inclined at 21°E to intersect perpendicular to the fault (Figures 1a and 1b). The borehole was fully cored using core liners to protect the cored samples and drilled with air to avoid contamination and destabilization of the borehole shale walls with mud or water. Then, it was left open for the tests. A 2.4 m long straddle packer interval was set across the fault, characterized by a lustrous and striated N0-to-170, 75-to-80°W surface to apply localized pressurization and to potentially reactivate the fault. Monitoring boreholes of 0.076-to-0.092 m diameter were spaced 1 to ~10 m from the injection hole to monitor pore pressures variations in the fault, strain, electrical resistivity, and induced seismicity concurrent with the experiment.

Within the ~2.4 m long testing interval, the structure is characterized by a strong dissymmetry of the tested fault zone. In the western compartment of the N0-to-170, 75-to-80°W main striated surface, there are almost no fractures. In the eastern compartment there is a 1 m thick highly fractured fault damage zone. Fractures display three principal orientations respectively of N110-to-140, 50°N-to-S, N160, 20-to-40W and N0-to-20, 40-to-80°W-to-E (Figures 1b–1d). The two first fracture sets are almost completely calcite filled and are crosscut by the third one (Figure 1d). The fault main plane is characterized by a polished but striated rough surface that cuts all the other fractures (Figure 1e). Inspection of the borehole wall by both borehole camera and by xCT-scan of the core shows that the surface displays some roughness at the intersection with the other fractures and that it is locally sealed with calcite.

2.2. SIMFIP Probe and Testing Method

The apparatus used for the step-pressure tests is composed of surface equipment to conduct the test and acquire the data, and a probe [*Guglielmi et al.*, 2013] (Figure 2). All the downhole equipment uses fiber-optic

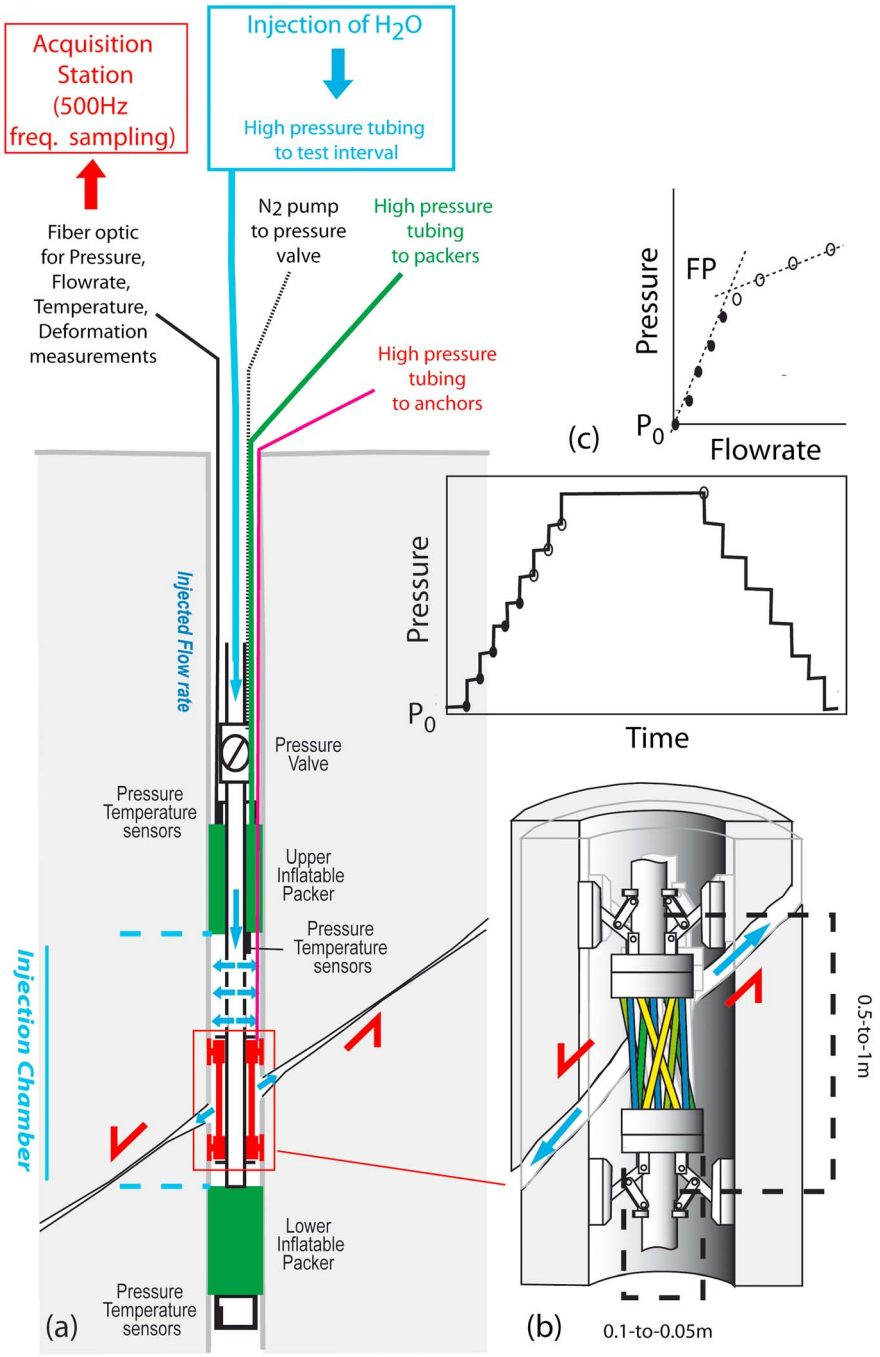

Figure 2. (a) SIMFIP test equipment setup. (b) Schematic view of the three-dimensional deformation unit. Tubes are differently colored to show that they display different deformations when there is a relative movement of the rings anchored to the borehole wall across the activated fracture. (c) Typical Step-Rate Test protocol.

sensors with reflection of light at specific wavelengths from fiber Bragg gratings manufactured by HBM (http://www.hbm.com) mounted between inflatable packers (red lines in Figure 2a). Thus, no downhole electrical supply is required. Sealing of the borehole test interval is accomplished by two inflatable rubber packers, spaced 2.4 m apart (straddle packer system).

To capture the three-dimensional deformation of the fault intersecting the borehole, an extensometer is centered along the axis connecting the two packers in the injection chamber (Figures 2a and 2b). Two fixed steel

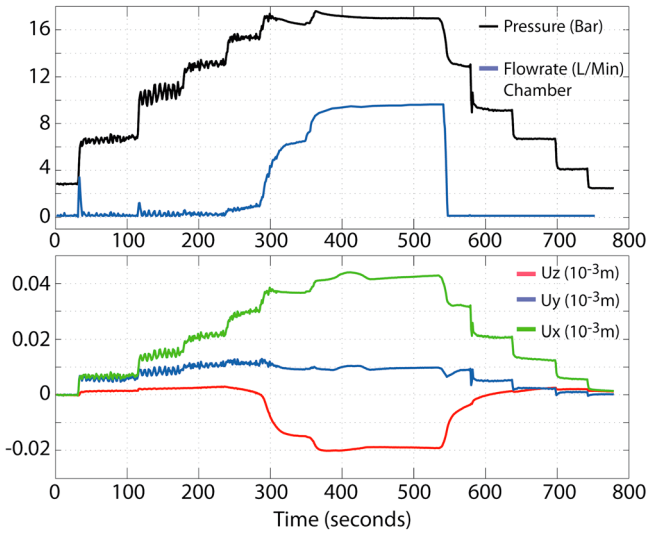

Figure 3. Variations of pressure- and flow rate -versus-time (upper graphs), and fault (U_x, U_y, U_z) hanging wall displacement-versus-time (lower graphs, orientation of the displacements is in Figure 1b).

rings are coupled to the borehole wall by hydraulically placed keys, which are run in on contact areas. Six small-diameter and deformable steel tubes connect the two rings with varying oblique orientations—making a cylindrical cage linking the upper and lower rings. This assembly forms the three-dimensional deformation measuring system—extension and torsion between the rings being uniquely resolvable by the extension of the six linking tubes. The rings are anchored to the borehole wall on each side of the fracture and are free to record the deformation of the borehole on either side of the fracture. The cage is 0.5 m long and 0.1 m diameter (Figure 2b). Tube deformations are captured with 10 fiber optic Bragg gratings that are attached to each tube and distributed along one single continuous fiber that brings the sensor signals to the surface-mounted data acquisition system, which is a MicronOptics dynamic optical interrogator (http://www.micronoptics.com). An inversion algorithm is used to calculate the relative three-dimensional displacements of the ring units from the tube deformations that are continuously monitored during the test. After laboratory calibrations of the probe response to pressure, stress/strain, and temperature, the displacement range is 0.7 and 3.5 mm in the axial and radial directions of the borehole, respectively, and the accuracy is 10^{-6} m. Attached to the straddle packer system is a magnetic orienting tool used to provide positioning of fault movements with a 0.1° accuracy.

Fluid pressure sensors independently monitor pressure variations in the test interval as well as above and below the straddle packer—as a guard against leakage from the zone (Figure 2a). The straddle packer system is made of two 0.102 m diameter and 1.3 m long BIMBAR dilatable hoses connected with a 0.04 m diameter central pipe. It is manufactured by Petrometalic company (http://en.petrometalic.com/). The BIMBAR sleeves are made of layers of steel cable imbedded into natural rubber, and the hoses were inflated with water to a pressure of 4 MPa during the test. The pressure sensors measure to 50 MPa allowing for high-pressure Step Rate Testing (SRT), and their 0.001 MPa accuracy can capture small pressure variations related to fracture movement. Temperature sensors are installed both within the interval and outside it to monitor the evolution of temperature during experiments with an accuracy of 0.1°C.

A downhole valve controls injection at the entrance to the test interval and is operated from the surface using gas (N_2) pressure conveyed downhole though a flexible hose (Figure 2a). First, packer inflation is hydraulically activated from the surface using water conveyed in flexible hoses. Second, the three-dimensional deformation cage is attached to the borehole wall by oil-pressure actuators supplied from the surface (Figure 2a).

During step rate tests, the water is injected at a low pressure for a fixed duration. The injection pressure is incremented and held constant, typically for the same duration. This is repeated while monitoring the deformations across the fault with the 3D deformation cage and sensors (Figure 2c). During the incremented pressure experiments each step lasted ~60 s. After reaching the fault opening pressure (FP), signaled by a large increase in flow rate at constant pressure (FP in Figure 2c), a 200 s long constant pressure injection

was conducted at a pressure above the fault opening pressure. This was then followed by successive step-down (decremented pressures) experiments until the pressure returned to its initial value. In the test protocol, pressure is imposed by the surface-mounted pump, while flow rate, injection chamber pressure, and displacement variations are monitored.

3. Results

The temporal evolution of gauge pressure and injected flow rate are shown in the upper panels of Figure 3. Variations in flow rate show a very different behavior during the pressure increments relative to the decrements:

1. From 0 to 237 s, the observed flow rate variations are related to pressure oscillations caused by the pump engine. No flow rate induced by diffusion in the formation is observed, while pressure is increased.
2. From 237 to 535 s, there is a large nonlinear flow rate increase initiating at 1.5 MPa. This corresponds to the pressure step-up period during which, between 450 and 535 s, a quasi-steady state hydraulic regime evolves in the fault characterized by quasi-constant flow rate and pressure, showing that the test has reached an external hydraulic (permeable) boundary. Indeed, outflows were measured at the monitoring wells R, S2, and S4, respectively, spaced 2, 7, and 9 m from the injection well (see Figure 1b and section 4.2 for a more detailed spatial analysis; measurements were performed manually at the wells head using a bowl that was weighted every 10 to 60 s).
3. From 535 to 547 s, although the pressure step-down protocol is similar to that for step-up, flow rate falls rapidly to zero at the onset of the pressure decrease from 1.7 to 1.4 MPa between 535 and 547 s (and while pumping is not stopped).
4. After 547 s, the test corresponds to a pressurized period without any flow injected in the fault.

The lower panels of Figure 3 show the temporal evolution of the three displacement components (U_x, U_y, and U_z) of western compartment (hanging wall) of the fault (the footwall is considered fixed). Fault displacements display close correlations with pressure variations characterized by maximum displacements (U_x, U_y, and U_z) $= (44.0 \times 10^{-6}\,\text{m},\ 10.5 \times 10^{-6}\,\text{m},$ and 20.0×10^{-6} m) at the maximum imposed pressure of 1.8 MPa and an almost complete resetting to zero initial displacement with residual displacements (U_x, U_y, and U_z) $= (1.4 \times 10^{-6}\,\text{m},\ 0.2 \times 10^{-6}\,\text{m},$ and $1.2 \times 10^{-6}\,\text{m})$ being only marginally above the 10^{-6} m measurement accuracy for the U_x and U_z components. Induced displacements are characterized by a shear component much larger than the normal component, the U_x and U_z components of fault movements, respectively, being a factor of 4 and 2 higher than the U_y component. Shear displacements are mobilized from the beginning of the test:

1. Before 237 s, while there is no apparent leakage into the fault, all three components of fault displacement increase with increasing fluid pressure.
2. After 237 s when injection into the fault begins to increase, there is an inversion of the vertical shear displacement U_z reversing sense as the pressure increases, and a 2-to-3 $\times 10^{-6}$ m normal closing in U_y.
3. Between 450 and 535 s, there are no fault movements when there is the quasi-steady state flow regime in the fault.
4. After 535 s, displacement occurs with the pressure decrements as the injected flow rate (Figure 3a) falls rapidly to zero. At this time, fault displacements are thus essentially induced by variations in effective stress when there is trapped water in the fault, and the pump only maintains pressure with no flow.

Figure 4a shows that the western compartment of the fault moving in the (U_y, U_z) plane perpendicular to the fault plane is first characterized by an initial opening almost perpendicular to the fault plane followed by normal slip with closing. These movements are associated with a large horizontal anticlockwise (left-lateral) slip in the (U_x, U_y) horizontal plane (Figure 4b) in close alignment with the measured directions of the principal horizontal stresses [*Cornet*, 2000]. During incremented pressure steps (in red), there is a variation in the fault normal component U_y characterized by progressive fault closing with the increase in the fault drainage that occurs with slip. At the completion of the step-up pressure period, the fault is almost closed. Then, a small pressure decrease similar to the one imposed at the onset of the step-down pressures (noted in the transition between red and green points in Figure 4) is sufficient to completely close the fault inducing the originally significant flow rate to fall to zero. After the closing of the fault, the presence of water "trapped" in the

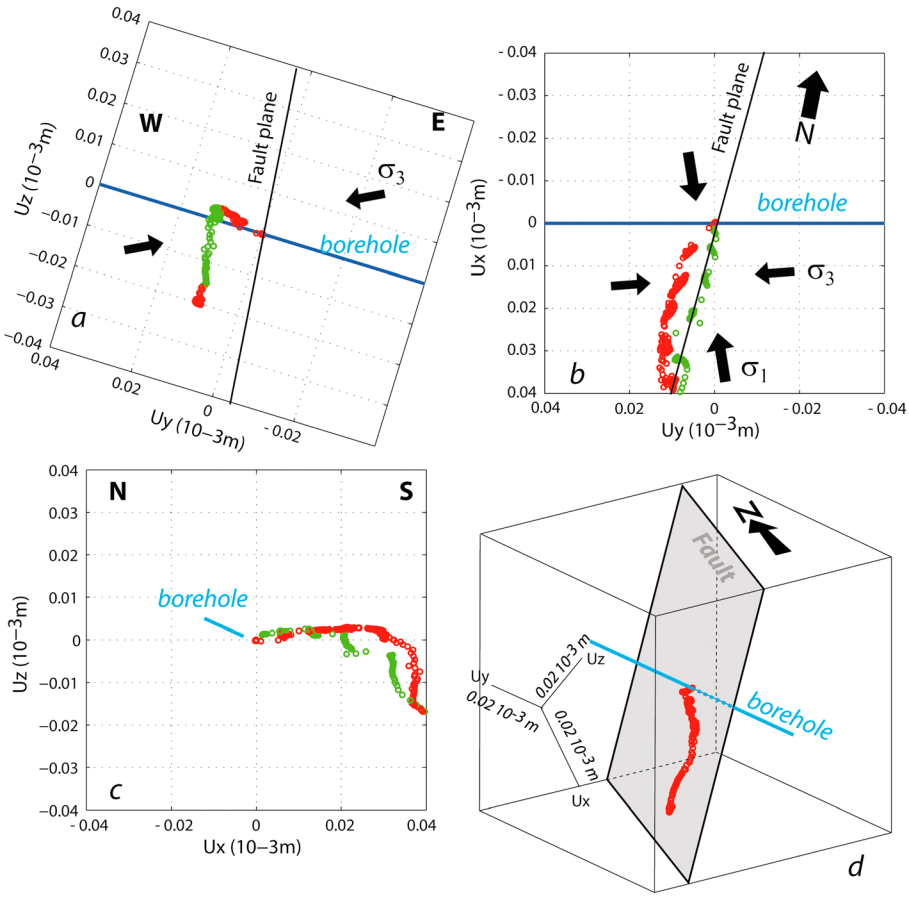

Figure 4. Three-dimensional displacements of the fault hanging wall (a) in the (U_y, U_z) plane, (b) in the (U_y, U_x) plane, (c) in the (U_x, U_z) plane, (d) in three-dimensions (red circles correspond to displacements induced by the step-up pressures, green circles correspond to displacements induced by the step-down pressures).

activated fault plane that modifies its rheology may explain the different path followed by fault displacements during the pressure step-down period (in green).

Figure 4c shows that above 1.3 MPa, there is a 22° rotation of the slip vector around the *x* axis in the (U_x, U_z) plane, which is parallel to the fault plane. At initial and final pressure steps lower than 1.3 MPa, fault movements are characterized by horizontal slip (U_x, U_y, and U_z) = (0.02×10^{-3} m, 0.01×10^{-3} m, and0.001×10^{-3} m). This movement, which occurs under zero-flow-rate conditions, may be related to (1) minor readjustment of the injection device, (2) borehole induced stress perturbations, and (3) complexity of the fault surface, which may contain asperities. Above 1.3 MPa, fault slip progressively rotates from 0 to 22° with the invasion of fluid into the fault. Differences in the movements induced during either incrementing or decrementing pressures highlight the complex dependency of fault movements on fault antecedent conditions, similar to the tenets of rate-state behavior.

Figure 5 shows the variations of slip movement and injected flow rate versus injected pressure. Above 0.8 MPa, (U_x, U_y, and U_z) displacements all display a linear variation with pressure until 1.5 MPa that results from the poroelastic response of the borehole and the surrounding medium, which includes the fault. Above 1.5 MPa, highly nonlinear displacements occur more or less independently of pressure variations. Displacements at high pressure induce an offset in the displacement-versus-pressure path, the displacements during the step-down pressures following a different path to that during the step-up pressures. The high increase in flow rate occurs mainly during this stage of fault displacement under high pressure, which is characterized by predominant normal slip (U_z negative variation) and a small contraction along the borehole axis (U_x negative variation). The contraction may result from minor fault closing or from a small (<10°)

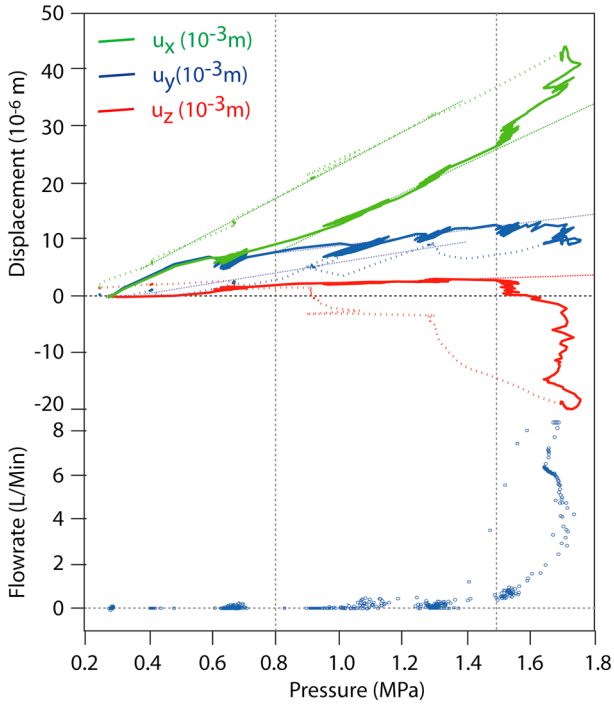

Figure 5. (top) (U_x, U_y, U_z) displacements and (bottom) flow rate versus the injected pressure.

angle between the borehole axis and the normal to the fault plane. Thus, the increase in hydraulic conductivity of the fault is related to shear when the fault is at incipient slip. In detail, step-down displacements below 1.5 MPa display linear variations in U_x and U_y with different slopes (dashed lines in Figure 5) compared to the step-up period, and a complex variation in U_z. This may be related either to damage of the fault stiffness that occurred during the high pressure inelastic period, or to different responses of the fault whether water is trapped or drained. Below 0.8 MPa, the almost complete return to the initial displacements may be explained (i) by local effects that predominate at or very near to the borehole walls, shadowing a significant part of the inelastic residual displacements or (ii) by a reversible movement on the activated fault.

4. Coupled Hydromechanical Numerical Analyses

4.1. Model Setting and Simulation Protocol

To rigorously analyze the coupled hydromechanical processes involved in the fault reactivation, we apply a three-dimensional coupled hydromechanical model accommodating the fluid pressure changes applied during the step-up SRT experiment (Figure 6). The distinct element code 3DEC [*Cundall*, 1988; *Itasca Consulting Group, Inc.*, 2003] is used to represent the fault as a discontinuity separating two compartments represented as two blocks that are free to move, rotate, and separate relative to one another. Contacts exist between the two deformable blocks at each node of the discontinuity. The program uses an explicit algorithm so that information propagates through the model dynamically (time domain dynamic algorithm). At each time step, the laws of motion and constitutive equations are jointly applied to calculate normal and shear forces at each contact, which then are used in the calculation of the block motion. The fault constitutive model is the generalization of the Coulomb friction law. In the elastic range, the fault behavior is governed by the fault normal and shear stiffnesses (units are Pa.m^{-1}), K_n and K_s as described by equations (1) and (2):

$$\Delta F^n = -K_n \Delta U^n A_c \tag{1}$$

$$\Delta F^s = -K_s \Delta U^s A_c \tag{2}$$

where A_c is the contact area, ΔU^n and ΔU^s are the normal and shear displacements increments, and ΔF^n and ΔF^s are the normal and shear force increments.

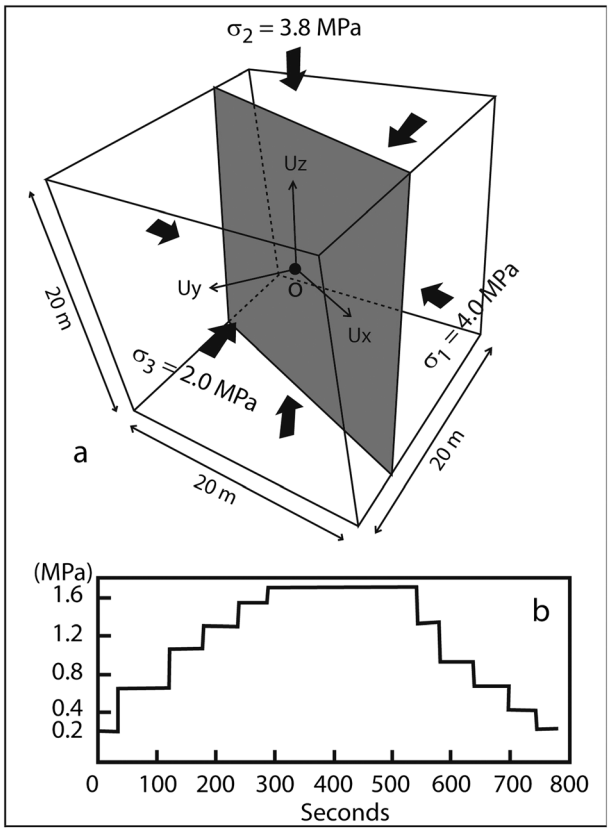

Figure 6. (a) Geometry of the numerical model and boundary conditions; (b) pressure variations imposed at point O in the model.

In the plastic range, both shear and tensile failure are considered, and joint dilation is included. The tensile normal force is limited to

$$T_{\max} = -TA_c \tag{3}$$

where T is the fault tensile strength.

The maximum sustainable shear force is given as

$$F^s_{\max} = cA_c + F^n \tan\varnothing \tag{4}$$

where c and $\varnothing$ are the fault cohesion and friction angle, respectively.

Once the onset of failure is identified at the subcontact, the tensile strength and cohesion are set to zero, this instantaneous loss of strength approximates the "displacement-weakening" behavior of the fault. Dilation occurs only as the fault slips, as defined in

$$\Delta U^n(dil) = \Delta U^s \tan\varphi \tag{5}$$

where φ is the dilation angle and ΔU^s is the shear displacement increment when fault slips.

In the model, fluid flow is represented within the fault alone, and not in the surrounding porous medium. The fault is represented as parallel-sided fracture with an equivalent hydraulic aperture u_h. Fluid flow rate per unit width of the idealized fracture follows the cubic law [*Witherspoon et al.*, 1980].

$$q = -\frac{u_h^3 \rho g}{12\mu}\nabla_h = \; -k_H \nabla_h \tag{6}$$

where k_H is the hydraulic conductivity of the fault (m/s), ∇_h is the gradient in hydraulic head, ρ is the fluid density (kg/m^3), g is the acceleration due to gravity (m/s^2), and μ is the fluid viscosity (Pa s).

To analyze the experimental results, two hydraulic conductivity-versus-stress relationships were considered for the fault. In the elastic range, the hydraulic conductivity varies as a function of the effective stress as [*Detournay*, 1980]

$$k_H = \frac{\rho g}{12\mu}(u_{h0} + \Delta U^n)^3 = \frac{\rho g}{12\mu}\left(u_{h0} + \frac{\Delta F^n}{A_c K_n}\right)^3 = \frac{\rho g}{12\mu}\left(u_{h0} + \frac{\Delta \sigma_n^{'}}{K_n}\right)^3 \tag{7}$$

where u_{h0} is the fault aperture at zero normal stress and $\Delta\sigma_n^{'}$ is the increment in the Terzaghi effective normal stress, which is written in simplified form as [*Walsh*, 1981]

$$\Delta\sigma_n^{'} = \; \Delta\sigma_n + \alpha\Delta P_p \tag{8}$$

where ΔP_p is the increment in the pore pressure and the effective stress coefficient $\alpha \sim 1$.

In the plastic range, the cubic law is adapted with the hydraulic conductivity of the fault varying (1) as a function of the effective stress ("elastic" equivalent hydraulic aperture u_{he}) and (2) as a function of dilation induced by fault slip ("slip" equivalent hydraulic aperture u_{hs}), as

$$k_H = \frac{\rho g}{12\mu}(u_{he} + u_{hs})^3 = \frac{\rho g}{12\mu}\left(u_{h0} + \frac{\Delta\sigma_n^{'}}{K_n} + u_{hs}\right)^3 \tag{9}$$

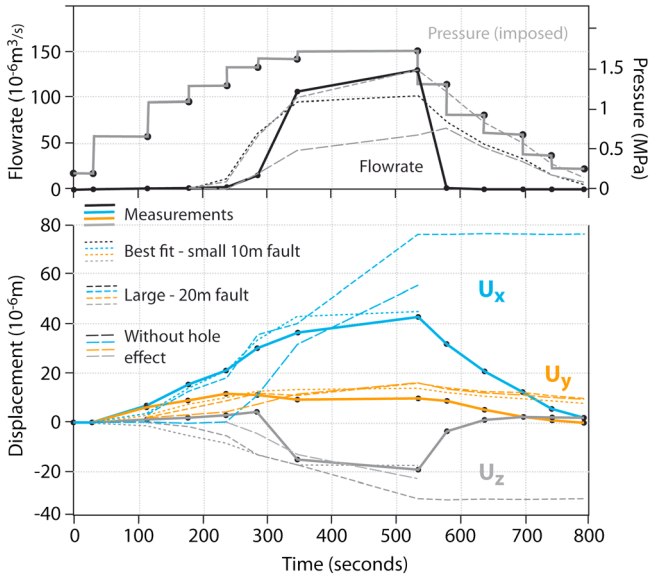

Figure 7. Best-fit numerical solutions of flow rate (upper graphs) and fault hanging wall displacements (lower graphs).

The analyses of the experimental data show that u_{hs} cannot be simply taken equal to the dilation induced at fault slip $\Delta U^n(dil)$, since the measured normal component during fault slip is very small (and/or negative) compared to the increase in u_{hs}. We thus considered the following simple relationship:

$$u_{hs} = B \times u_{he} \tag{10}$$

where B is evaluated as a function of the measured flow rate and pressure during the step rate experiment. Here $B \sim 7$ was recovered as the best match between experimental and calculated curves (see Figure 7) and included from beginning of the simulation. The key idea is to consider that flow in reality can only occur in fractured parts of the fault plane. Equation (7) describes flow related to the poroelastic opening of the preexisting (before the test) fractured parts of the fault plane, and equation (9) describes permeability enhanced by failure (either in shear or tension) of solid-to-solid contacts in the initially unfractured parts of the fault plane

The two fault compartments (footwall and hanging wall) and borehole are contained within a cube 20 m-on-edge centered on the intersection between the borehole and the fault (Figure 6a). The reactivated fault, which is the only discontinuity within the cube, separates the model into two blocks. The principal stresses measured by *Cornet* [2000] at the depth of the experiment are applied to the six faces of the cube domain. An in situ stress

Table 1. Best-Fit Model Properties

Material	Parameter	3DEC Best Fit Values
Fault	Normal stiffness, K_n (GPa/m)	200
	Shear stiffness, K_s (GPa/m)	4
	Cohesion, c (Pa)	0
	Static friction angle, $\varnothing$ (°)	35.0
	Dilation angle, ϕ (°)	5.0
	Initial Hydraulic aperture, u_{h0} (m)	1.7×10^{-5}
	Hydraulic aperture at slip, u_{hs} (m)	12×10^{-5}
Rock matrix	Bulk modulus, K_R (GPa)	5.15
	Shear modulus, G_R (GPa)	3.94
	Mass density, ρ_R (kg/m^3)	2500
	Permeability, k_R (m^2)	0
Fluid	Mass density, ρ_F (kg/m^3)	1000
	Bulk modulus, K_F (GPa)	2
	Dynamic viscosity, μ_F (Pa/s)	1×10^{-3}

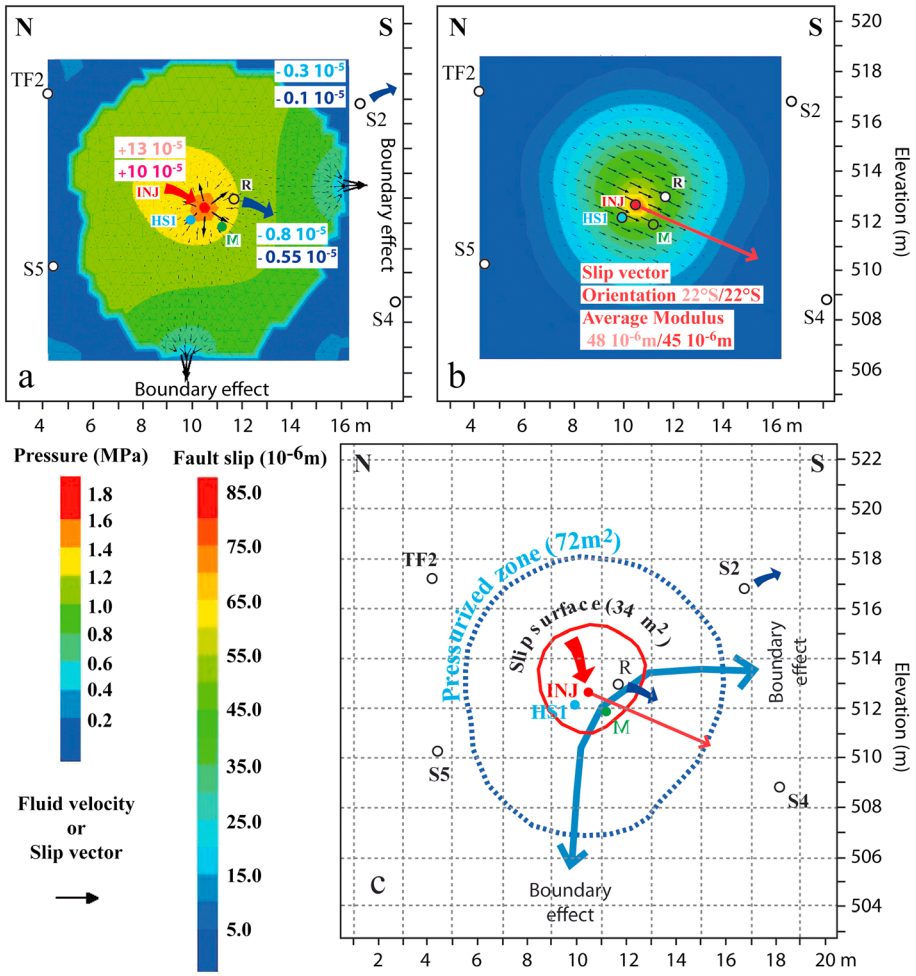

Figure 8. Calculated (a) pressure (red arrow is the injection, blue arrows are the observed outflows at adjacent monitoring holes, values are in m^3/s and light is measured, and dark is calculated) and (b) displacement fields in the plane (U_x, U_z) of the fault—light is measured; dark is calculated. (c) Synthetic view of both pressure and displacement fields boundaries (small circles correspond to intersections between boreholes and the fault plane).

gradient is set according to the weight of the rock with an in situ pore pressure of 0.4 MPa set in the fault. This is congruent with long-term measurements recovered by IRSN [*Dick et al.*, 2013] in the same fault zone at a distance of about 100 m. With these stress conditions, normal stress across the fault is assumed to be of 2.0-to-2.2 MPa around the injection point. The field experiment is simulated by imposing a time-dependent pressure step increase at the fault grid point coordinates (0, 0, 0) corresponding to the step-rate pressure history imposed in the borehole straddle packer interval during the in situ experiment (Figure 6b). Flowrate injected into the fault is then calculated from observed pressure gradients around grid point (0, 0, 0) and the permeability evaluated from the relative (U_x, U_y, U_z) displacements of the fault-hanging wall toward the footwall. The model is first run to equilibrium then pressures are step-incremented with time as a point source in the center of the model—coordinates (0, 0, 0) from which fluid then radiates.

The modeling procedure comprises two steps:

1. Fault stiffness (K_n, K_s), static friction angle, and transmissivity variations were first estimated using the three-dimensional fully coupled hydromechanical solutions. Using the best fit solution(s), the relationships between fault slip, pore pressures, and discharge rate history were then investigated in time and in the fault plane.
2. Finally, a sensitivity analysis was conducted to investigate the effects of the fault hydromechanical parameters, pressure, and stress conditions on fault reactivation.

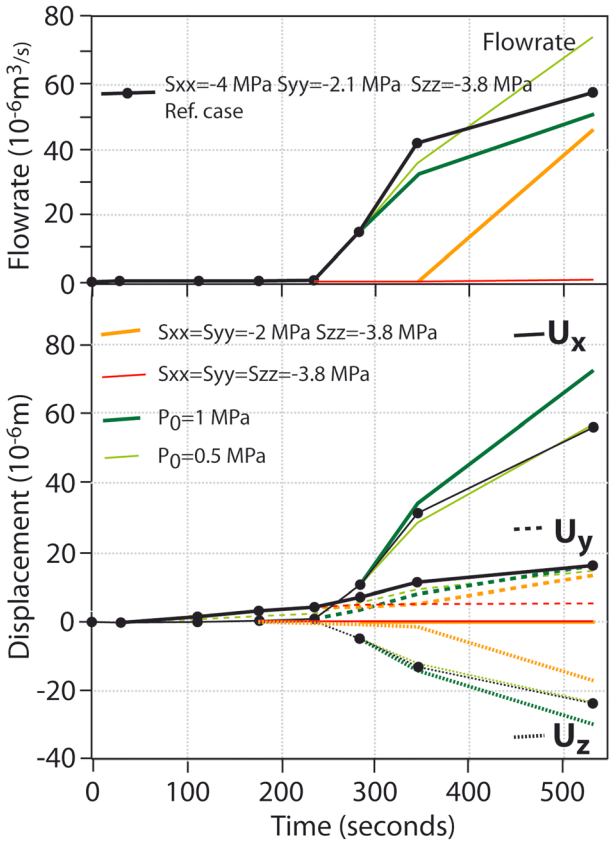

Figure 9. Variation of fault displacements as a function of stress.

4.2. Modeling Results

Figure 7 shows three model solutions that reasonably match both measured fault movements and injected flow rate. The best fit is obtained when a low static friction angle of 22° is applied in a fault area of diameter 0.5 m centered around the injection point with a 35° friction angle set in the far field. A reduced size model 10 m × 10 m on-edge is considered for this (see—Best fit—small 10 m fault in Figure 7 and Table 1).

For all three components of displacement, the (U_x, U_y, U_z) calculated orientations match the measurements during the incremented pressure step portion of the STR test. For decreasing pressures, the experiment is poorly matched by the models which all display a large residual inelastic displacement and a progressive decrease in flow rate compared to the measurements, which include a reverse slip and a sharp decrease in flow rate to zero. Such a discrepancy between model and measurements illustrates that slip along the pre existing fault, the only physics considered in the model, is not the only mechanism occurring in situ. Indeed, the role of mode 1 opening/closing and poroelastic effects that can occur on other connected fractures or on branches of the isolated portion of the fault tip may explain the reverse slip of the fault. Additionally, flow is described merely by a simple parallel plate model for permeability (no channeling is considered) and a residual hydraulic aperture prevents flow from falling to zero as it is the case in the field—that may also be in error.

The comparison between the cases both with and without the low near-field fault friction angle (respectively the "Best fit" and "Without hole effect" cases in Figure 7) shows that before 237 s, measurements are dominated by the near-field or centimeter-scale effects close to the borehole wall. This is normal as, given the low initial fault conductivity, the zone invaded by the fluid pressure is restricted to very close to the borehole wall. A reduction of fault friction in the area close to the borehole allows a significant improvement in matching model with measurements. Regardless, it produces only very localized failure of the fault at low injection pressures. This may not completely reflect the physics of displacement-versus-pressure below 1.5 MPa in better accordance with some linear poroelastic response of the fault. In addition, if the low 22° friction angle is applied to the entire fault (instead of 35°), there is a large overestimation of fault movement at high pressures and at times exceeding 250 s (see chapter 4.3). Such analyses highlight that fault response close to the borehole may be principally related to near borehole stress perturbations and/or to the effects of the straddle packer system. Indeed, if the stress perturbations induced by the open hole on the fault are negligible, it can be calculated that pressurization of a finite borehole between the straddle packer systems may influence both the axial and radial stresses [*Gan and Elsworth*, 2013], inducing a significant decrease in the fault normal stress and increase in the fault shear stress. This may thus explain the high elastic response of the fault to low injected pore pressures at early stages of injection when the invasion of the fluid pressure into the fault is too limited to significantly induce any change in effective stress on the fault.

A comparison between the large 20 m × 20 m and the small 10 m × 10 m models (respectively "Large-20 m fault" and Best fit cases in Figure 7) show that the size of the model and thus hydraulic boundary effects

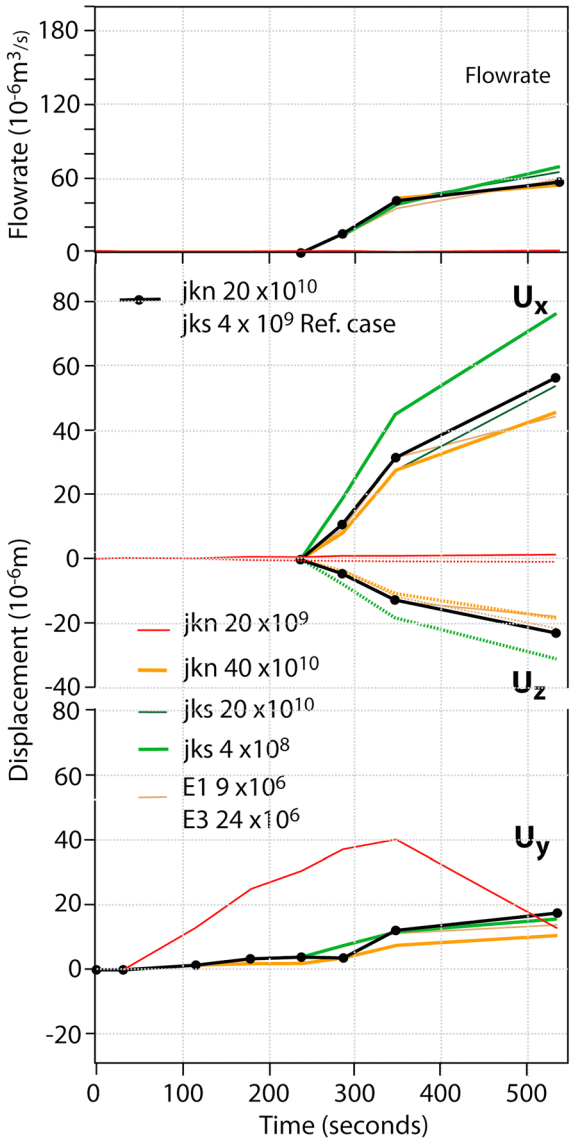

Figure 10. Variation of fault displacements as a function of fault elastic properties.

influence the test after 500 s. The large model induces an overestimation of fault shear displacements U_x and U_z while matching the measured flowrates. The small fault model best fits the shear displacements and only slightly underestimates the injected flow rate. Considering the fault geology of Figure 1, there is a high potential that multiple branching occurs along the same fault zone or that the fault is connected with other faults at distances of 5 to 10 m from the injection hole. If hydraulically connected these other fault elements or networked faults could provide constant pressure boundaries, which would mean that they are more permeable than the injected fault. Another possibility is that dilatancy at fault tips or on these faults increases their permeability enough for them to play the role of a constant hydraulic head boundary. This second possibility would also match the observed reverse slip effects previously discussed.

In Figure 8a, the calculated pressure field in the small fault model shows that at 500 s the pressure gradient in the fault is controlled by drainage at the south and basal model boundaries where flow velocities converge to a constant pressure boundary of 0.4 MPa. The boundary of the calculated pressurized zone is restricted to ~1.5 ± 0.5 m inside the area bounded by the intersections of fault surface with monitoring holes S2, S4, S5, and TF2. This shows that either the model underestimates the pressurized area of the fault or that the pressurized area in situ displays a much more complex shape than that calculated. Complexity within the fault drainage is suggested by leakage that was observed from boreholes R, S2, and S4—showing flow channeling that occurs preferentially toward the south of the fault plane. In that direction, the calculated flow rates match measurements reasonably well for boreholes R and S2. Drainage toward the base of the model was not observed in the field since no leakage occurred out of boreholes M and HS1 located below the injection hole. Regardless, when comparing the injected flow rate of 13×10^{-5} m^3/s with the cumulative measured value of 1.3×10^{-5} m^3/s at R and S2 (S4 outflow was too small to be measured), it appears that a large fraction of the injected water drainage was not apparent at the monitoring holes.

Figure 8b shows that fault slip is focused in the less well drained northern upper quadrant of the fault, which is more highly pressurized than the southern lower block. The calculated orientation and magnitude of the slip vector and modulus match the measured slip, with values respectively of 22° toward the south and of 45×10^{-6} m compared to 48×10^{-6} m, respectively. The slipping patch has an area of ~34 m^2, its geometry and location strongly constrained by the effects of hydraulic boundaries to the fault that create preferential flow channeling where pore pressures are too low to promote slip. In Figure 8c, it is striking to observe that the flow channel orientation is almost perpendicular to the slip direction, its geometry being influenced by movement along the fault.

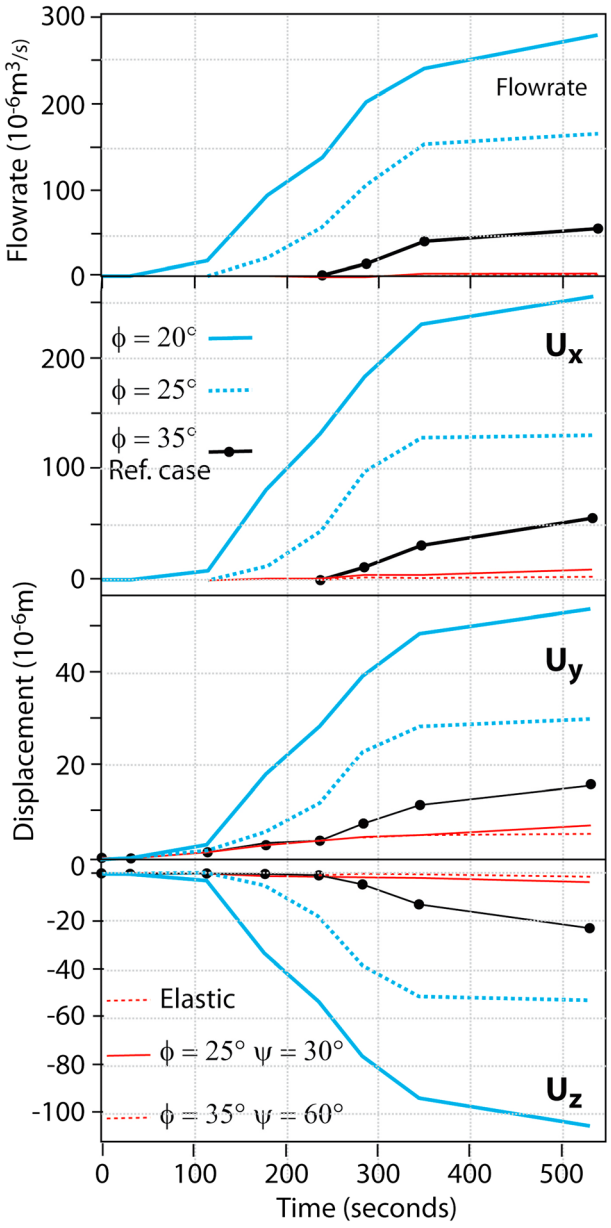

Figure 11. Variation of fault displacements as a function of fault friction.

4.3. Sensitivity Study

In Figure 7, we showed that both flow rate and fault displacements could be matched with a simple Coulomb stress hydromechanical model of a fault isolated within a 10 m × 10 m block. Although some of the fault physics such as (1) the off-fault dilatant effects and (2) the near-borehole effects were not captured by this model, we focused on the sensitivity of this simple analysis to the different model parameters. We compared the effects of these parameters on model results taking the case of the fault without the influence of the borehole (Figure 7) as the reference case.

4.3.1. Effects of the Regional Stress Regime and of Initial Pore Pressure

In Figure 9, we consider different states of stress on the fault—respectively, a normal stress regime and an isotropic stress regime. We compare this to the strike-slip stress regime determined in situ [*Cornet*, 2000] and considered in the best fit case (Figure 7). In all models, the orientation of the stress tensor was unchanged with σ_{yy} stress being almost perpendicular to the fault plane (Figure 6a). Stress magnitudes were varied within the range of accuracy of the in situ values, which is characterized by a 50% accuracy in the determination of the horizontal stress components caused by difficulties in imaging the hydraulic fractures in the shale materials after the leak-off tests [*Cornet*, 2000]. If horizontal stresses are set to a value of 3.8 MPa, equal to the vertical stress (isotropic stress regime, red curves in Figure 9), then there is no fault slip and only a very small variation in flow rate. This model shows that the variation of the hydraulic aperture of the fault that is associated with variations in effective stress in the elastic range is small compared to variations induced by fault slip. If both principal horizontal stresses are set equal to 2.1 MPa and lower than σ_{zz} = 3.8 MPa (normal stress regime, orange curves in Figure 9), the shear components U_x and U_z of fault displacements and associated flow rate are underestimated, and variations occur about 100 s later at injected pressures higher than in the best fit case, respectively, of 1.73 compared to 1.52 MPa. These two models allow the differentiation between the respective contributions of the horizontal and normal slip components in associated hydraulic aperture increase in the fault while, in both cases, fault slip occurred at the same calculated effective normal stress value of 1.86 MPa. The strong coupling between hydraulic aperture related to horizontal slip favors an early invasion of fluid into the fault plane, which modifies the effective normal stress in an area large enough to induce the initiation of fault rupture under a lower injection pressure than in the case of a "simple" biaxial normal stress regime. These analyses are of importance to show that the value of the

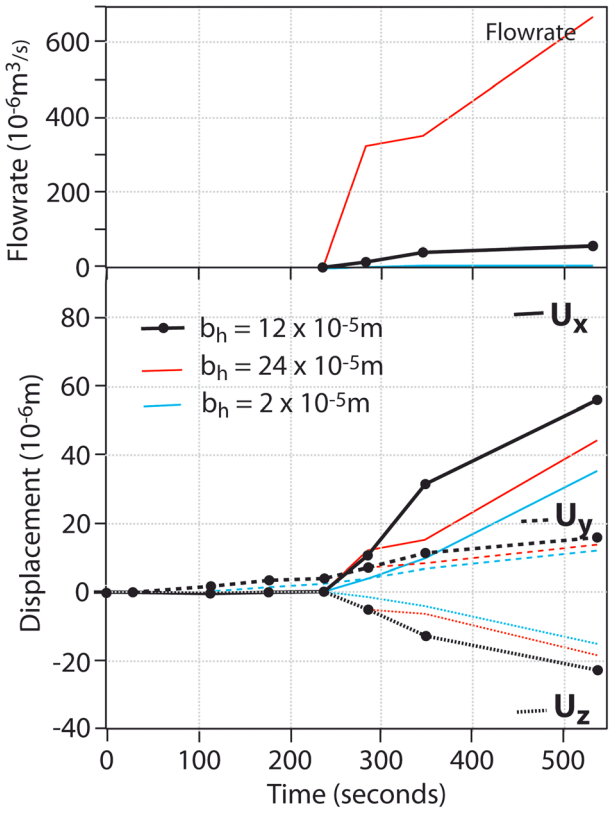

Figure 12. Variation of fault displacements as a function of fault hydraulic aperture.

fluid pressure at failure may not be equal to the normal stress because of the strong coupling between shear failure and variations in fault permeability.

A significantly higher initial value of the formation pressure, respectively, of 1 MPa compared to the best fit value of 0.4 MPa does not significantly affect fault displacements but does induce a smaller increase in flow rate (green curves in Figure 9). This shows that at high initial pore pressures, the smaller hydraulic gradient imposed in the fault has a minor effect on effective stress variations inducing failure but a large effect on Darcy flow in the fault.

4.3.2. Effects of the Fault Elastic and Strength Properties

A factor of 10 lower fault normal stiffness ($K_n = 20 \times 10^9$ Pa/m in Figure 10 compared to best fit value $K_n = 20 \times 10^{10}$ Pa/m) induces a high normal deformation but inhibits fault slip, and thus, there is a very small increase in flow rate (similar to the case of isotropic elastic stress in Figure 9). A factor of 10 reduction in fault shear stiffness (compared to best fit value $K_s = 4 \times 10^9$ Pa/m) slightly increases shear displacements and flow rate, while an increase in the stiffness or of imposing elastic anisotropy of the intact rock slightly decreases fault displacements. Nevertheless, the minor influence of variations in elastic properties on the hydromechanical behavior of the fault at failure may be biased by the very simple Coulomb rupture constitutive relationships used in the model. Indeed, Figure 11 (blue curves) shows that when the static friction angle is lowered from 35 to 22°, there is a large increase in slip in the U_x and U_z components and failure occurs earlier at lower effective stress variations. Since the variation in hydraulic aperture of the fault is conditioned by fault slip in the model, the variation in flow rate closely mirrors fault slip. A large dilation angle of 60° (Figure 11, red curves) does not play a major role on failure and flow rate variations showing that variations in fault hydraulic conductivity cannot be described by a simple dilation effect related to shear on the slipping plane. These models show that simple Coulomb failure dominated by stress and friction may reasonably represents fault slip activation.

4.3.3. Effects of the Fault Hydraulic Properties

When the hydraulic aperture at failure u_{hs} (equations (9) and (10)) is increased by a factor of 2 ($u_{hs} = 24 \times 10^{-5}$m in Figure 12 red curves compared to best fit value $u_{hs} = 12 \times 10^{-5}$m), there is a factor of 100 increase in the flow rate according to the calculated opening implemented in the "cubic" law of this model. This increase in flow rate dampens the pressure variation on the fault plane and moderates the variation in effective stress that then gives an underestimate of fault normal opening and shear slip. When u_{hs} is lowered by a factor of 12 ($u_{hs} = 2 \times 10^{-5}$m in Figure 12 blue curves), flow rate increases but is very small and initiates only minor invasion of pressure into the fault plane. Because it is restricted to only a small area of the fault plane, the limited increase in effective stress traction results in highly underestimated fault displacement. These results show that coupling flow rate with measurements of fault movement allows an accurate estimation of the variation of fault hydraulic properties with stress, highlighting the strong influence of hydraulic conductivity on fault rupture initiation.

5. Discussion

5.1. Capturing Fault Slip

The Step-Rate Injection Method for Fracture In Situ Properties (SIMFIP) method used in this experiment appears to be a promising in situ method to improve the estimation of stress magnitudes and their three-dimensional orientations in and around a fault zone. Since it couples a direct monitoring of three-dimensional fault movements with fluid pressures and injected flow rate to produce micrometer-scale fault displacements, this method is complementary to field hydraulic methods such as leak-off tests, minifracs and hydraulic fracturing [*Haimson and Cornet*, 2003], and to laboratory methods such as anelastic stress recovery [*Lin et al*., 2006]. We show that a preexisting fault can be moved by tens of microns, i.e., significantly above the accuracy of the instrument, at imposed pressures below the fracturing pressure. Compared to sensors that measure normal deformation of horizontal preexisting natural fractures [*Schweisinger et al*., 2007] or radial displacements caused by a hydrofracture creation [*Lin and Ray*, 1994] both in vertical to subvertical wellbores, the SIMFIP sensor captures three-dimensional movements whatever the orientations of both wellbore and existing fractures may be. The analyses show that measurements conducted at low imposed pressures and at the beginning of the test are complex because they are influenced by many parameters such as the instrument stiffness, the borehole strength, and the local perturbation of the stress state. This justifies extending the method to higher pressure steps and longer durations to better capture intrinsic fault properties and effective stress variations, which are not affected by the borehole. Before 237 s the response of the strain sensor to borehole pressurization steps is immediate and flow rate is below measurement threshold, which suggests the displacements observed correspond to an immediate and undrained poroelastic response of a borehole drilled through an heterogeneity. In fact, borehole near-field deformation is probably predominant in the measured strain until the fault opening pressure is reached, which we also interpret as the threshold for shear failure.

One acceptable criterion to estimate whether local borehole effects are minimized is to slowly increase pressures until there is a linear correlation both between the imposed fluid pressures and measured (crack-opening) displacements and between the imposed fluid pressures and the injected flow rate. At this time, the test allows the capture of the poroelastic response of the fault before failure. When the duration of the experiment is extended, some hydraulic boundaries may influence the signals because an in situ fault is a structure of finite size that is eventually connected to other faults. This gives the opportunity to explore both properties of the tested fault before the boundary effect is felt and to determine properties at larger scale—as complementary to laboratory scale studies.

We show that estimating the normal stress on the fault from only the fault-opening-pressure (FP in Figure 2) may lead to a significant (17%) underestimation because the effects of shear displacements on fault pressures (caused by the increase in fault conductivity under shear) are neglected. Indeed, direct reading of field data give a FP of 1.4 to 1.7 MPa, while the best fit normal stress is estimated at 1.86 MPa. The coupled numerical analyses of the FP, associated (U_x, U_y, U_z) values and flow rate variations show that the measured signals are sensitive to many parameters. These include the effective horizontal stress magnitudes and orientations, strength properties of the fault and the strength of couplings between displacements and fault invasion by the pressurized fluids. The interpretation can then face a nonunique solution, but we show that processes interact at the different times during the test that can schematically be divided into several periods [*Guglielmi et al*., 2013]:

1. The initial undrained period before fluids have significantly penetrated the fault. This period is strongly influenced by presence of the borehole and may eventually be used to characterize borehole stresses and strength as well as the poroelastic properties of the fault.
2. The drained poroelastic period when fluids invade the fault before failure. This period is characterized by both a linear variation of displacements with the imposed pressure and a linear variation of the injected flow rate with the imposed pressure, which allows estimation of the elastic properties of the fault (this period is represented in the test between 1 and 1.4 MPa).
3. The rupture and drainage period (when the fault slips and its hydraulic conductivity drastically increases). Models show that rupture can be described by a static Coulomb criterion, thus allowing the estimation of fault peak static friction as well as the normal and shear stresses applied on the fault plane.
4. The undrained poroelastic period when fluids are trapped in the closed fault that is still pressurized during the step-down of imposed pressures. The transition between this period and the previous gives a second possibility to estimate fault strength and state of stresses.

5.2. In Situ Hydromechanical Properties of Faults in Shales

The fault elastic normal and shear stiffness respectively of 200 and 4 GPa/m appear highly contrasted, showing that the fault is prone to a much higher elastic deformation in shear than in the normal direction. This may be explained by recent works on nanostructures of faults in shales that show a thin coating on the fault surface characterized by a rearrangement of clay minerals parallel to the fault surface and an almost complete initial closing that introduces weak transverse elastic fault properties [*Laurich et al.*, 2014]. On one hand, such contrast may favor the accumulation of elastic shear strain and an increase in shear stress at the boundaries of the pressurized patch in the fracture plane before rupture. Alternatively, the magnitude of the normal stiffness, which is about 5 times higher than that of more permeable fractures in carbonate reservoirs [*Cappa et al.*, 2006; *Worthington and Lubbe*, 2007; *Guglielmi et al.*, 2008], may reflect a difference in the contact area between the two fault walls being much larger for faults in shale compared to faults in carbonates. This may be because aligned clay mineral surfaces have more adhesion to one another than carbonate minerals or this could result from a smaller size of zones without contact on faults in shales than in limestones. The normal stiffness of a crack is inversely proportional to its diameter [*Kachanov*, 1993]. Thus, the stiffness of a fracture is expected to depend not only on the relative surface of open versus contact areas but also on the length scale of the open areas. Then, the effective normal stress may vary much less during pressurization because a limited area of the fracture surface is in contact with water.

The static peak friction coefficient of 0.67 estimated from the in situ experiment appears relatively high compared to values deduced from double direct shear tests conducted in the laboratory on clay-rich fault gouge [*Haines et al.*, 2013]. These show intrinsically low and/or drastic friction decreases at low shear strains due to the presence of phyllosilicate-rich materials that rapidly localize deformation into thin surfaces. Although the activated fault displays a local polished and striated surface apparently indicative of a low friction coefficient, the high friction (at the meter-to-decameter test scale) highlights potential friction strengthening of clay faults. Different processes can be invoked (1) such polished surfaces correspond to patches where the fault is thin (micrometer aperture) enough to retain solid-solid contacts and promoting high surface energy sites that favor healing processes [*Niemeijer et al.*, 2008], (2) the calcite sealing of large aperture zones that is observed in many shale fractures (and in the other fractures intersected by the test interval) may affect the fault surface in other zones than the one intersected by the borehole, and (3) fault asperity amplitudes, which are the scale of the induced fault displacements, may constrain the slip.

There is a factor of 7 increase in the hydraulic aperture that is clearly related to the activation of slip on the fault. At low effective normal stresses (~1–2 MPa), variations in hydraulic conductivity of clay fractures may result from a complex combination of the swelling of clay minerals, consolidation and creep [*Gutierrez et al.*, 2000; *Bastiaens et al.*, 2007]. Few data constrain the evolution of hydraulic conductivity in clay fractures with shear. Some recent laboratory experiments show that conductivity may decrease initially at low shear strain then increase at high strains through the development of auxiliary fractures out of the main shear plane [*Cuss et al.*, 2011]. The first results from this field experiment indicate that an exponential (or multilinear) permeability-versus-Coulomb stress relation may be applied to describe permeability evolution of faults in shale at low shear strains (equation (9)). Compared to laboratory hydro-shearing experiments conducted on Opalinus clay fractures by *Cuss et al.* [2011], we show much higher increases in conductivity (2 orders of magnitude compared to 1 order of magnitude observed in the laboratory) for much lower shear displacements, i.e., about 0.2×10^{-3} m compared to 5×10^{-3} m in the laboratory.

Following *Rutqvist et al.* [1998], a very low fault storativity (S) can be approximated using equation (11):

$$s\approx\frac{\gamma}{k_n}=\frac{9.8}{200\times10^{9}}=0.05\times10^{-9} \tag{11}$$

where γ is the specific weight of water and k_n is the fracture normal stiffness. Provided hydraulic transmissivities ranging between 10^{-19} and 10^{-20} $m^2 s^{-1}$ measured on similar clay fault material [*Faulkner and Rutter*, 2000; *Nussbaum and Bossart*, 2004; *Dick et al.*, 2013], the initial fault hydraulic diffusivity D can be approximated using equation (12):

$$D=\frac{T}{S}=\frac{10^{-19}\ to\ 10^{-20}}{0.05\times10^{-9}}=2.0\times10^{-9}\ \text{to}\ 10^{-10}\ m^2s^{-1} \tag{12}$$

If we convert the ×7 increase in hydraulic aperture estimated from the Tournemire fault activation test into a transmissivity using the cubic law (equation (6)), we obtain a value of $T=7\times10^{-6}$ m^2s^{-1}. Considering that

variations in fault storativity are negligible, we get a fault diffusivity $D = 3.5 \times 10^3$ $m^2 s^{-1}$ during fault slip. There are very few hydraulic diffusivity values estimated in situ on active faults. The value that we determined is much higher than $D = 7 \times 10^{-5}$ $m^2 s^{-1}$ estimated after the Chichi earthquake at about 1.1 km on the Chelungpu fault, which is in silty shales of the Chinshui formation [*Doan et al.*, 2006]. Although the Chelungpu tests corresponded to cross-hole hydraulic tests between two holes separated by 40m, i.e., a decameter scale in the same range as the Tournemire experiment (~10 to 20 m), the two faults are of different sizes, architectures, and experienced different slip magnitudes under different state of stresses. Nevertheless, if we consider the Tournemire fault as one structure in a large-scale fault damage zone, our results show that very fast pressure diffusion could occur over decameters under infra-millimeter-scale stress/strain variations such as the ones occurring during a rupture nucleation phase.

6. Conclusion

Field reactivation experiments on the Tournemire fault provide new observations showing that faults in shales may display complex behavior. In particular, this includes substantial increases in permeability induced by relatively very small, inframillimeter, slip movements. This is, to our knowledge one of the first in situ measurement of permeability evolution coupled to fault movement at rupture, as typical field experiments performed on fault drilling projects in the best cases give properties of the fault either before or after its activation [*Kitagawa et al.*, 1999; *Doan et al.*, 2006; *Cornet et al.*, 2004]. We find that a pressurization of the fault to ~40% of the lithostatic pressure induces a significant increase in hydraulic diffusivity in shale to values of 10^3 $m^2 s^{-1}$ that are firmly in the range of those observed in deep crystalline rock masses [*Townsend and Zoback*, 2000]. This is also in good accordance with another experiment of fault activation in carbonates that has been conducted with the same equipment and protocol showing a 14-fold increase of the fault permeability associated to a 1.2 mm dilatant slip event [*Guglielmi et al.*, 2015].

Importantly, our results suggest complex processes of permeability increase related to fault shear that create a large additional hydraulic aperture for fluid flow, which is not reflected in the total normal displacement as measured over the 2.4 m wide borehole interval. Indeed, these field measurements are done for shear displacements of tens of microns associated to a small dilatancy and possibly even a progressive closing of the fault after slip initiation. It is very tiny although we calculate that a high permeability zone is reached within a radius of several meters around the injection pressure source. This suggests the opening of localized conduits (rather than a global fault opening), which generates a nonuniform radial flow along the fault that strongly controls slip. When the fault is depressurized there is a sudden closing of the flow paths associated with back slip on the fault that highlights the importance of bulk poroelastic strain in disconnecting hydraulic paths between these dilatant zones and the pressure source. Our observations are thus complementary to observations at laboratory scale [*Faoro et al.*, 2009; *Cuss et al.*, 2011] and to models deduced from the analyses of calcite-filled strike-slip faults [*Petit et al.*, 1999], highlighting the influence of off-fault hydromechanical processes on dynamic variations of permeability with fault activation. Since the flow dimensions related to the size and connectivity of the different fractures in the fault damage zones may be a controlling parameter competing with stress effects, it is important that pressure step-rate tests be systematically performed to best estimate the changes in permeability related to fault activation. Usual tests performed at "constant" pressures in faults may underestimate the potential coupling between permeability variations and fault slip. Indeed, tests performed after a large earthquake measure the effects of damage on permeability, rather than the potential of permeability variations under fault slip.

The experiment shows that a small amplitude slip of tens of micrometers can be produced on a 30-to-50 m^2 patch in a fault that is critically stressed. In turn, this slip depends strongly on the diffusion speed of the fluid, here estimated at 0.013 m/s corresponding to a slow aseismic slip event that lasted about 215 s. Although distinguishing inelastic rupture effects is difficult given the small magnitude of the measured deformations and their almost complete apparent reversibility, such signals may represent analogues to study slow slip events in the near-surface and their role in the seismic nucleation on faults that can be induced by natural stress instabilities or engineered injections into the deeper crust. Our results also show that the migration of fluids along very low diffusivity faults may be quite easily favored by such slow aseismic slip on faults.

The in situ protocol presented in this paper thus provides new possibilities to study the interactions between nucleation and fault rupture and the migration fluids in fault zones intermediate between laboratory and full crustal scales. Longer duration experiments at high flowrates but controlled injection pressures appear as a promising way to capture larger slip and thus to study in the field the conditions for faults stability.

Acknowledgments

This work is supported by TOTAL Company within the framework of the "Fluid and Fault" project (PI is Raymi Castilla). The authors thank the IRSN (French Institute of Radioprotection and Nuclear Safety) for giving their dedicated help and the access to the IRSN Tournemire underground laboratory. We also deeply thank Patrice Desveaux who makes everything work on the site. The SIMFIP device is codeveloped between the CEREGE, SITES SAS, and Petrometalic companies under cofundings from the ADEME (French Agency of Environment and Energy). We thank H. Caron (technical head of SITES), Y. Zouhair (SITES engineer), H. Lançon (SITES engineer), and J.B. Janovczyck (Technical head of Petrometalic) for building and operating the instrument that made possible these experiments. Finally, the authors thank Chris Marone from Penn State University (USA) for fruitful discussions about the geomechanical modeling of the experiment. All experiment data are housed in the CEREGE laboratory, Aix-Marseille University, France (contact guglielmi@cerege.fr).

References

Archambault, G., S. Gentier, J. Riss, and R. Flamand (1997), The evolution of void spaces (permeability) in relation with rock joint shear behavior, *Int. J. Rock. Mech. Min. Sci.*, *34*, 3–4.

Bastiaens, W., F. Bernier, and X.-L. Li (2007), SELFRAC: Experiments and conclusions on fracturing, self-healing and self-sealing processes in clays, *Phys. Chem. Earth*, *32*, 600–615.

Boisson, J. Y., L. Bertrand, J. F. Heitz, and Y. Moreau-Le Golvan (2001), In situ laboratory investigations of fluid flow through an argillaceous formation at different scales of space and time, Tournemire tunnel, southern France, *Hydrogeol. J.*, *9*, 108–123.

Bonin, B. (1998), Deep geological disposal in argillaceous formations: Studies at the Tournemire Test Site, *J. Contam. Hydrol.*, *35*, 315–330.

Boutt, D. F., et al. (2012), Scale dependence of in-situ permeability measurements in the Nankai accretionary prism: The role of fractures, *Geophys. Res. Lett.*, *39*, L07302, doi:10.1029/2012GL051216.

Brown, S. R., and R. L. Bruhn (1998), Fluid permeability of deformable fracture networks, *J. Geophys. Res.*, *103*, 2489–2500, doi:10.1029/97JB03113.

Bruhn, R. L., W. T. Parry, W. L. Yonkee, and T. Thompson (1994), Fracturing and hydrothermal alteration in normal fault zones, *Pure Appl. Geophys.*, *142*, 609–644.

Cabrera, J., P. Volant, C. Baker, W. Pettitt, and R. P. Young (1999), Structural and geophysical investigations of the EDZ (Excavation Disturbed Zone) in indurated argillaceous media: The tunnel and the galleries of the IPSN Tournemire site (France), in *37th U.S Rock Mechanics Symposium*, edited by V. Amadei et al., pp. 957–964, Balkema, Vail, Colo.

Cabrera, J., C. Beaucaire, G. Bruno, L. De Windt, A. Genty, N. Ramambasoa, A. Rejeb, S. Savoye, and P. Volant (2001), Tournemire Project – Synthesis of 1995-to-1999 research programs, IPSN Rep. DPRE/SERGD 01–19, 202 pp.

Caine, J. S., J. P. Evans, and C. G. Foster (1996), Fault zone architecture and permeability structures, *Geology*, *24*(11), 1025–1028.

Cappa, F. (2009), Modeling fluid transfer and slip in a fault zone when integrating heterogenous hydromechanical characteristics in its internal structure, *Geophys. J. Int.*, *178*, 1357–1362.

Cappa, F., Y. Guglielmi, J. Rutqvist, C.-F. Tsang, and A. Thoraval (2006), Hydromechanical modelling of pulse tests that measure fluid pressure and fracture normal displacement at the Coaraze Laboratory site, France, *Int. J. Rock. Mech. Min. Sci.*, *43*(7), 1062–1082.

Charpentier, D., D. Tessier, and M. Cathelineau (2003), Shale microstructure evolution due to tunnel excavation after 100 years and impact of tectonic paleo-fracturing, Case of Tournemire, France, *Eng. Geol.*, *70*, 55–69.

Chen, N., W. Zhu, T. F. Wong, and S. Song (2005), Hydromechanical behavior of country rock samples from Taiwan Chelungpu Drilling Project, *Eos Trans. AGU*, *86*(52), Fall Meet. Suppl., Abstract T51A-1324.

Constantin, J., J. B. Peyaud, P. Vergély, M. Pagel, and J. Cabrera (2004), Evolution of the structural fault permeability in argillaceous rocks in a polyphased tectonic context, *Phys. Chem. Earth*, *29*, 25–41.

Constantin, J., P. Laurent, P. Vergély, and J. Cabrera (2007), Paleo-deviatoric stress magnitudes from calcite twins and related structural permeability evolution in minor fault: Example from the toarcian shale of the French Causses Basin, Aveyron, France, *Tectonophysics*, *429*, 79–97.

Cornet, F. H. (2000), Détermination du champ de contrainte au voisinage du laboratoire souterrain de Tournemire, Rapport du Laboratoire de Mécanique des Roches, Département de Sismologie, Institut de Physique du Globe de Paris, Rapport N°98N33/0073.

Cornet, F. H., M. L. Doan, I. Moretti, and G. Borm (2004), Drilling through the active Aigion Fault: The AIG10 well observatory, *C. R. Geosci.*, *336*(4–5), 395–406.

Coyle, B. J., and M. D. Zoback (1988), In situ permeability and fluid pressure measurements at approximately 2 km depth in the Cjon Pass research well, *Geophys. Res. Lett.*, *15*, 1029–1032, doi:10.1029/GL015i009p01029.

Cundall, P. A. (1988), Formulation of a three-dimensional distinct element model – Part I: A scheme to detect and represent contacts in a system composed of many polyhedral blocks, *Int. J.Rock Mech. Min. Sci. Geomech. Abstr.*, *25*, 107–116.

Cuss, R. J., A. Milodowski, and J. F. Harrington (2011), Fracture transmissivity as a function of normal and shear stress: Firs results in Opalinus Clay, *Phys. Chem. Earth*, *36*, 1960–1971.

Davis, E. E., K. Becker, K. Wang, and B. Carson (1995), Long-term observations of pressure and temperature in Hole 892B, Cascadia accretionary prism, in *Proceedings of the Ocean Drilling Program*, *Sci. Results*, edited by B. Carson et al., pp. 299–311, Ocean Drilling Program, College Station, Tex.

Davis, E. E., K. Wang, R. E. Thomson, K. Becker, and J. F. Cassidy (2001), An episode of seafloor spreading and associated plate deformation inferred from crustal fluid pressure transients, *J. Geophys. Res.*, *106*, 21,953–21,963, doi:10.1029/2000JB000040.

Detournay, E. (1980), Hydraulic conductivity of closed rock fracture: an experimental and analytical study, in *Proceedings of the 13th Canadian Rock Mechanics Symposium*, pp. 168–173, Univ. of Toronto, Ont., Canada.

Dick, P., C. Wittebroodt, M. Lefevre, C. Courbet, and J. M. Matray (2013), Estimating hydraulic conductivities in a fractured shale formation from pressure pulse testing and 3D modeling, AGU, Fall Meeting 2013, abstract MR11A-2202.

Doan, M. L., E. E. Brodsky, Y. Kano, and K. F. Ma (2006), In situ measurement of the hydraulic diffusivity of the active Chelungpu Fault, Taiwan, *Geophys. Res. Lett.*, *33*, L12317, doi:10.1029/2006GL026889.

Evans, J. P., C. B. Forster, and J. V. Goddard (1997), Permeability of fault-related rocks, and implications for hydraulic structure of fault zones, *J. Struct. Geol.*, *19*, 1393–1404.

Faoro, I., A. Niemeijer, C. Marone, and D. Elsworth (2009), Influence of shear and deviatoric stress on the evolution of permeability in fractured rock, *J. Geophys. Res.*, *114*, B01201, doi:10.1029/2007JB005372.

Faulkner, D. R., and E. H. Rutter (2000), Comparisons of water and argon permeability in natural clay-bearing fault gouge under high pressure at 20 degrees C, *J. Geophys. Res.*, *105*, 16,415–16,426, doi:10.1029/2000JB900134.

Faulkner, D. R., C. A. L. Jackson, R. J. Lunn, R. W. Schlische, R. W. Shipton, C. A. J. Wibberley, and M. O. Withjack (2010), A review of recent developments concerning the structure, mechanics and fluid flow properties of fault zones, *J. Struct. Geol.*, *32*, 1557–1575.

Gan, Q., and D. Elsworth (2013), Breakdown Pressures due to Infiltration and Exclusion in Finite Length Boreholes, 47th U.S. Rock Mechanics/Geomechanics Symposium, San Francisco, Calif.

Ge, S., and S. C. Stover (2000), Hydrodynamic response to strike slip and dip–slip faulting in a half space, *J. Geophys. Res.*, *2000*, 25,513–25,524, doi:10.1029/2000JB900233.

Gudmundsson, A., S. S. Berg, K. B. Lyslo, and E. Skurtveit (2001), Fracture networks and fluid transport in active fault zones, *J. Struct. Geol.*, *23*, 343–453.
Gudmundsson, A., T. H. Simmenes, B. Larsen, and S. L. Philipp (2010), Effect of internal structure and local stresses on fracture propagation, deflection and arrest in fault zones, *J. Struct. Geol.*, *32*, 1643–1655.
Guglielmi, Y., F. Cappa, J. Rutqvist, C. F. Tsang, and A. Thoraval (2008), Mesoscale characterization of coupled hydromechanical behavior of a fractured-porous slope in response to free water-surface movement, *Int. J. Rock. Mech. Min. Sci.*, *42*, 852–878.
Guglielmi, Y., F. Cappa, H. Lançon, J. B. Janowczyk, J. Rutqvist, C. F. Tsang, and J. S. Y. Wang (2013), ISRM suggested method for Step-Rate Injection Method for Fracture In-Situ Properties (SIMFIP): Using a 3-components borehole deformation sensor, *Rock. Mech. Rock Eng.*, *47*, 303–311, doi:10.1007/s00603-013-0517-1.
Guglielmi, Y., F. Cappa, J. F. Avouac, P. Henry, and D. Elsworth (2015), Seismicity triggered by fluid injection-induced aseismic slip, *Science*, *348*(6240), 1224–1226.
Gutierrez, M., L. E. Øinob, and R. Nygardc (2000), Stress-dependent permeability of a mineralised fracture in shale, *Mar. Pet. Geol.*, *17*, 895–907.
Haimson, B. C., and F. H. Cornet (2003), ISRM suggested methods for rock stress estimation – Part 3: hydraulic fracturing (HF) and/or hydraulic testing of pre-existing fractures (HTPF), *Int. J. Rock Mech. Min. Sci.*, *40*, 1011–1020.
Haines, S. H., B. Kaproth, C. Marone, D. Saffer, and B. van.der Pluijm (2013), Shear zones in clay-rich fault gouge: A laboratory study of fabric development and evolution, *J. Struct. Geol.*, *51*, 206–225.
Hedan, S., P. Cosenza, V. Valle, and J. Cabrera (2011), Caractérisation par extensométrie optique de la fracturation liée à la désaturation de l'argilite de Tournemire: Impact de l'hétérogénéité et de l'anisotropie structurale, 20ème Congrès Français de Mécanique.
Henry, P. (2000), Fluid flow at the toe of the Barbados accretionary wedge constrained by thermal, chemical, and hydrogeologic observations and models, *J. Geophys. Res.*, *105*, 25,855–25,872, doi:10.1029/2000JB900215.
Husen, S., and E. Kissling (2001), Postseismicfluid low after the large subduction earthquake of Antofagasta, Chile, *Geology*, *29*, 847–850.
Itasca Consulting Group, Inc. (2003), *3DEC 3-Dimensional Distinct Element Code*, ICG, Minneapolis.
Kachanov, M. (1993), Elastic solids with many cracks and related problems, *Adv. Appl. Mech.*, *30*, 259–445.
Kitagawa, Y., N. Koizumi, K. Notsu, and G. Igarashi (1999), Water injection experiments and discharge changes at the Nojima Fault in Awaji Island, Japan, *Geophys. Res. Lett.*, *26*, 3173–3176, doi:10.1029/1998GL005263.
Laurich, B., J. L. Urai, G. Desbois, C. Vollmer, and C. Nussbaum (2014), Microstructural evolution of an incipient fault zone in Opalinus Clay: Insights from an optical and electron microscopic study of ion-beam polished samples from the Main Fault in the Mt-Terri underground research laboratory, *J. Struct. Geol.*, *67A*, 107–128.
Lin, P., and T. G. Ray (1994), A new method for direct measurement of In-Situ stress directions and formation rock properties, *SPE J. Petrol. Technol.*, *46*, 249–254.
Lin, W., M. Kwasniewski, T. Imamura, and K. Matsuki (2006), Determination of three-dimensional in-situ stresses from anelastic strain recovery measurement of cores at great depth, *Tectonophysics*, *426*, 221–238, doi:10.1016/j.tecto.2006.02.019.
Mitchell, T. M., and D. R. Faulkner (2009), The nature and origin of off-fault damage surrounding strike-slip fault zones with a wide range of displacements: a field study from the Atacama fault system, northern Chile, *J. Struct. Geol.*, *31*(8), 802–816, doi:10.1016/j.jsg.2009.05.002.
Mitchell, T. M., and D. R. Faulner (2008), Experimental measurements of permeability evolution during triaxial compression of initially intact crystalline rocks and implications for fluid flow in fault zones, *J. Geophys. Res.*, *113*, B11412, doi:10.1029/2008JB005588.
Muir-Wood, R., and G. C. P. King (1993), Hydrological signatures of earthquake strain, *J. Geophys. Res.*, *98*, 22,035–22,068, doi:10.1029/93JB02219.
Niemeijer, A. R., C. Marone, and D. Elsworth (2008), Healing of simulated fault gouges aided by pressure solution: Results from rock analogue experiments, *J. Geophys. Res.*, *113*, B04204, doi:10.1029/2007JB005376.
Nussbaum, C., and P. Bossart (2004), Compilation of K-values from packer tests in the Mont Terri rock laboratory, Tech. Note 2005–10, Mont-Terri Project, Geotechnical Institute Ltd., Switzerland.
Olsson, W. A., and S. R. Brown (1993), Hydromechanical response of a fracture undergoing compression and shear, *Int. J. Rock Mech. Min. Sci. Goemech. Abstr.*, *30*(7), 845–851.
Petit, J. P., C. A. J. Wibberley, and G. Ruiz (1999), 'Crack-seal', slip: a new fault valve mechanism?, *J. Struct. Geol.*, *21*(8–9), 1199–1207.
Rutqvist, J., C.-F. Tsang, and O. Stephansson (1998), Determination of fracture storativity in hard rocks using high pressure testing, *Water Resour. Res.*, *34*, 2551–2560, doi:10.1029/98WR01863.
Rutqvist, J., J. Birkholzer, F. Cappa, and C.-F. Tsang (2007), Estimating maximum sustainable injection pressure during sequestration of CO2 using coupled fluid flow and geomechanical fault-slip analysis, *Energy Convers. Manage.*, *48*, 1798–1807.
Schweisinger, T., L. Murdoch, and C. Huey (2007), Removable Borehole Extensometers for Measuring Axial Displacements during Well Tests, *Geotech. Test. J.*, *30*(3), doi:10.1520/GTJ100576.
Townsend, J., and M. D. Zoback (2000), How faulting keeps the crust strong, *Geology*, *28*(5), 399–402.
Tremosa, J., D. Arcos, J. M. Matray, F. Bensenouci, E. C. Gaucher, C. Tournassat, and J. Hadi (2012), Geochemical characterization and modelling of the Toarcian/Domerian porewater at the Tournemire underground research laboratory, *Appl. Geochem.*, *27*, 1417–1431.
Walsh, J. B. (1981), Effect of pore pressure and confining pressure on fracture permeability, *Int. J. Rock Mech. Min. Sci. Geomech. Abstr.*, *18*, 429–435.
Wang, C.-Y., L.-H. Cheng, C.-V. Chin, and S.-B. Yu (2001), Coseismic hydrologic response of an alluvial fan to the 1999 Chi-Chi earthquake, Taiwan, *Geology*, *29*, 831–834.
Wibberley, C. A. J., and T. Shimamoto (2003), Internal structure and permeability of major strike-slip fault zones: the Median Tectonic Line in Mie Prefecture, Southwest Japan, *J. Struct. Geol.*, *25*, 59–78.
Witherspoon, P. F., J. S. Y. Wang, K. Iwai, and J. E. Gale (1980), Validity of cubic law for fluid flow in a deformable rock fracture, *Water Resour. Res.*, *16*, 1016–1024, doi:10.1029/WR016i006p01016.
Worthington, M. H., and R. Lubbe (2007), The scaling of fracture compliance, *Geol. Soc. London Spec. Publ.*, *270*, 73–82.
Zhang, S., T. E. Tullis, and V. J. Scruggs (1999), Permeability anisotropy and pressure dependency of permeability in experimentally sheared gouge materials, *J. Struct. Geol.*, *21*, 795–806.